

**REPORT DOCUMENTATION PAGE**

18

Public reporting burden for this collection of information is estimated to average 1 hour per response, including the time for reviewing instructions, searching existing data sources, gathering and maintaining the data needed, and completing and reviewing this collection of information. Send comments regarding this burden estimate or any other aspect of this collection of information, including suggestions for reducing this burden to Department of Defense, Washington Headquarters Services, Directorate for Information Operations and Reports (0704-0188), 1215 Jefferson Davis Highway, Suite 1204, Arlington, VA 22202-4302. Respondents should be aware that notwithstanding any other provision of law, no person shall be subject to any penalty for failing to comply with a collection of information if it does not display a valid OMB control number. **PLEASE DO NOT RETURN YOUR FORM TO THE ABOVE ADDRESS.**

<b>1. REPORT DATE (DD-MM-YYYY)</b> 18-02-2008	<b>2. REPORT TYPE</b> Final	<b>3. DATES COVERED (From - To)</b> 06/15/2007-11/30/2007
<b>4. TITLE AND SUBTITLE</b>  <b>Modeling of Interactions of Ablated Plumes</b>		<b>5a. CONTRACT NUMBER</b>
		<b>5b. GRANT NUMBER</b> <b>AFOSR FA9550-07-1-045</b>
		<b>5c. PROGRAM ELEMENT NUMBER</b>
<b>6. AUTHOR(S)</b> PI Alex Povitsky		<b>5d. PROJECT NUMBER</b>
		<b>5e. TASK NUMBER</b>
		<b>5f. WORK UNIT NUMBER</b>
<b>7. PERFORMING ORGANIZATION NAME(S) AND ADDRESS(ES)</b>  The University of Akron                      The University of Akron, Akron, OH, USA		<b>8. PERFORMING ORGANIZATION REPORT NUMBER</b>
<b>9. SPONSORING / MONITORING AGENCY NAME(S) AND ADDRESS(ES)</b> AFOSR 875 N Randolph St Arlington VA 22203  Dr John Schmissieur/NA		<b>10. SPONSOR/MONITOR'S ACRONYM(S)</b> John D. Schmissieur
<b>12. DISTRIBUTION / AVAILABILITY STATEMENT</b>  Approved for public release, distribution unlimited		<b>11. SPONSOR/MONITOR'S REPORT NUMBER(S)</b>
<b>13. SUPPLEMENTARY NOTES</b>		

20080404115

**14. ABSTRACT** Heat transfer modulation between the gas flow and the Thermal Protection Shield (TPS) that occurs because of ejection of under-expanded pyrolysis gases through the cracks in the TPS is studied by numerical modeling. The simulations are performed for an axisymmetric bluff body flying at Mach 7. The influence of the geometry of the TPS on heat transfer pattern was studied for two representative shapes. The results are presented for three different flight altitudes (low-ground level, moderate-20km and high-30km). At the low altitude the plume pressure is lower than the pressure behind the detached front shock wave and the plume propagates slowly along the wall surface. At high and moderate altitudes, the plume path and consequently, convective heat transfer between the TPS and the plume depends on the plume interaction with the bow shock wave. The effect of initial pressure of pyrolysis gas on the plume dynamics is significant. The presence of the blast wave associated with under-expanded plume alters the heat transfer and increases mixing. Finally, the enhanced heat transfer caused by the emergence of multiple plumes is investigated.

**15. SUBJECT TERMS**

Ablation, plumes, interaction of shock waves, Godunov scheme, altitude of flight, pyrolysis

**16. SECURITY CLASSIFICATION OF:**

a. REPORT

b. ABSTRACT

c. THIS PAGE

**17. LIMITATION  
OF ABSTRACT**

**18. NUMBER  
OF PAGES**

17

**19a. NAME OF RESPONSIBLE PEI**  
Povitsky

**19b. TELEPHONE NUMBER (include  
code)**  
330-972-2685

Standard Form 298 (Rev. 8-98)  
Prescribed by ANSI Std. Z39.18

**Personnel supported: PI Prof. Alex Povitsky, graduate student Kedar Pathak**

**Publications pertinent to the grant from the beginning of grant in June 2007:**

- A. Povitsky, K. Pathak and D. Gaitonde, Dynamics of Multiple Plumes Generated by Local Injection of Ablated Material, the 46<sup>th</sup> AIAA Aerospace Sciences Meeting and Exhibit, Reno, January 2008, AIAA Paper 2008-0577, to be submitted to AIAA Journal
- B. N. Mullenix and A. Povitsky, Comparison of Hertz-Knudsen and Ytrehus Carbon Ablation Rates Using a Reactive-Riemann Solver, the 46<sup>th</sup> AIAA Aerospace Sciences Meeting and Exhibit, Reno, January 2008, AIAA paper 2008-1222, to be submitted to J. of Thermophysics and Heat Transfer
- C. K. Pathak and A. Povitsky, Multi-time Step Modeling of Plume Dynamics in Carbon Ablation, accepted for publication in Journal of Nanoscience and Nanotechnology , January 2008.

**Nomenclature**

$E$	= total energy per unit mass
$g$	= vector of fluxes in the radial direction
$l_{visc}$	= viscous length scale; $l_{visc} = \sqrt{\nu t}$
$M$	= Mach number
$p$	= pressure
$Q_0$	= normalization parameter for heat transfer



$Q$	= heat transfer
$T_w$	= temperature at the wall surface
$T_{NW}$	= temperature at the control volume next to the wall
$t$	= time
$u$	= axial velocity
$v$	= radial velocity
$w$	= vector of fluxes in the axial direction
$x$	= axial coordinate
$y$	= radial coordinate
$\nu$	= kinematic viscosity

## I. Introduction

Extensive research has been conducted in predicting the ablation rates of Thermal Protective Shield (TPS) due to hypersonic flow around aerospace vehicles. When subjected to increasing heat flux or temperature, thermal protection materials may pyrolyze and/or ablate. Pyrolysis is chemical decomposition in the interior of a TPS material, which releases gaseous by-products without consuming atmospheric species. Ablation is a combination of vaporization, sublimation, and reactions (such as oxidation) which converts solid surface species into gaseous species<sup>1</sup>. The majority of published ablation and pyrolysis studies are limited to the set-up of uniformly distributed ablated mass flux that varies gradually along the TPS surface and does not cause separation of the boundary layer.

Local non-uniform ablation can produce local plumes having much higher pressure, injection speed, and density compared to those corresponding to the average ablation speed under the same flight conditions. The severely under-expanded gas escapes through the cracks as a series of high-pressure plumes. Small scale but high-intensity phenomena such as locally non-uniform mass transfer across the TPS surface can greatly affect the overall flowfield about the vehicle, transition to turbulence, heat exchange between the gas surrounding the vehicle and the TPS surface, and the overall ablation and pyrolysis rates. Escape of pyrolysis gases dramatically changes the surface temperature and can trigger transition to turbulence<sup>2</sup>. Prior studies regarding this transition to turbulence caused by pyrolysis are based on uniform diffusion of the produced gas through micro-pores and not through macro-cracks resulting from spallation (that is, formation of cracks through which the pyrolysis gas escapes)<sup>3,4,5</sup>. The current study is aimed at modeling of the heat transfer modulation caused by the local plume(s) emergence for the range of flight altitude, initial plume pressure and the shape of the TPS. The fluid dynamics of plume is much more involved compared to the extensively studied "jet in cross-flow" set-up because of (i) interaction of pyrolysis plume with the detached bow shock wave in hypersonic flight and (ii) enhanced mixing of plume with surrounding gas because of the pressure wave associated with the under-expanded plume.

Emerging plumes can alter the pressure gradient and the shape of velocity profile around the TPS causing formation of a separation vortex with enhanced convective heat transfer from the hypersonic flow to the TPS. On the one hand, intense cooling from pyrolysis gases may increase thermal stresses and enhance spallation. On the other hand, in principle pyrolysis gases can be used for desired cooling of the TPS if their escape routes are properly organized. Overall, the local heat- and mass- transfer processes will be greatly amplified in comparison to those in the laminar boundary layer of regular ablation. Modeling and scaling of these phenomena is one future step in the current research that will map out the uncharted regimes beyond spatially homogeneous ablation.

The recent research of the authors in numerical modeling of laser ablation<sup>6,7</sup> developed the needed numerical methodology and physical understanding of dynamics of under-expanded microsecond-scale laser-ablated plumes thus assisting in solving the current problem.

One reason for non-uniform ablation is impingement of solid objects such as debris, ice, and/or foam into TPS elements<sup>8</sup>. Another reason is the formation of cracks and gas escape routes because of the nature of TPS materials at high temperature. The pyrolysis gas of carbon-phenolic TPS can be approximately considered a mixture of H, H<sub>2</sub>, CO, and CH<sub>4</sub><sup>9</sup>. The temperature of pyrolysis gas ranges from 800K at the inner surface to 1800K at the outer surface of pyrolysis zone, based on flight thermocouple data for Pioneer-Venus<sup>10</sup>. Pyrolysis gas pressure inside the TPS of Pioneer-Venus is between 8 and 30 atm for the four Venus vehicles (see Ref. 11). Such a high internal pressure in pyrolysis layer induces spallation. The observed rough surface with deep cracks in TPS confirms the importance of modeling of non-uniform ablation.

Formatted: Endnote Reference

Deleted: 9

Deleted: 9

Formatted: Endnote Reference

View of a charring ablator with the millimeter-scale cracks after a test in the VKI Plasmatron is shown in Refs.<sup>10,11</sup> The typical size of cracks that appear because of intensive heating is of the order of millimeters<sup>10,11</sup> and this size was adopted in the current study.

In a more broad sense, the size of initial plume diameter ranges from microns to centimeters depending on whether the ablated gas escapes through the pores in the TPS material or its ablation is caused by mechanical damage. In a composite, the space scales range from individual fiber diameter (7 $\mu$ m) to the apparent diameter of tows and warps (300-500 $\mu$ m)<sup>12,13,14</sup>. On the limit of small scales of cracks, carbon-carbon composites can generally contain a significant initial amount of cracks, voids and de-bonded fiber/matrix interfaces, which can yield a porosity level as high as 20%. The typical size of cracks/voids is 14 micron and the size of de-bonded interfacial gaps is 0.5 micron<sup>15</sup>. On the other hand, the mechanical damage to the TPS may cause formation of much larger local intense ablation spots in the TPS<sup>16</sup>.

The report is organized as follows. In Section 2, the mathematical model and numerical method used are described. In Section 3, the modeled effect of flight altitude on the plume dynamics and heat transfer is discussed. In Section 4, the role of initial pressure of pyrolysis gases is described. The injection of multiple pulses is presented in Section 5. In Section 6, the influence of the shape of the TPS on the plume interactions is obtained.

## II. Description of Model

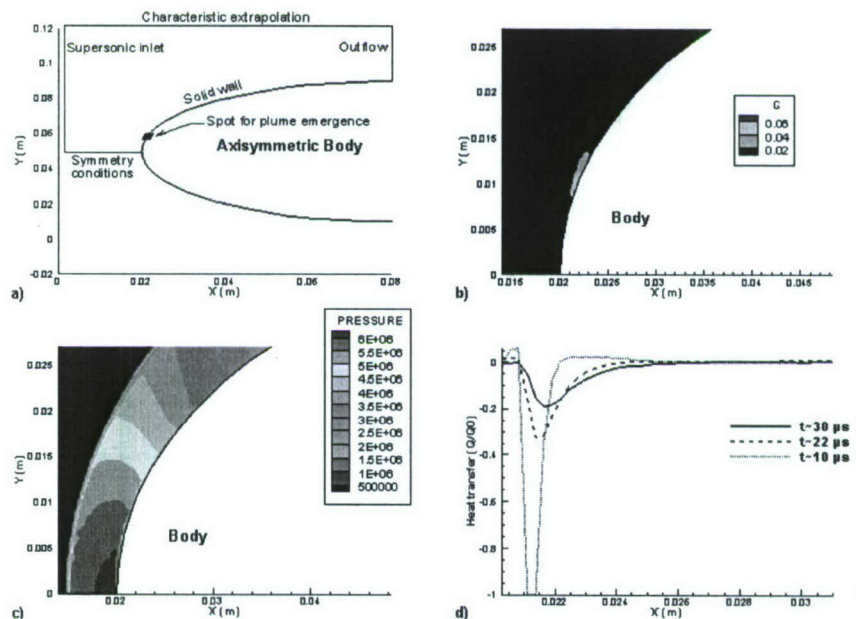


Figure 1. Schematic of the problem for flight at the ground level: a) the shape of the representative TPS and computational domain, b) plume concentration, c) pressure distribution, and d) heat transfer at the TPS wall.

### A. Conditions of flight and emerging plume

The Mach number of flight for the current study is  $M = 7$ . The axisymmetric ellipsoid bluff TPS shape chosen for this study is shown in Fig. 1a. The plume emergence for the TPS shape considered in Ref.<sup>17</sup> is studied in Section 6. For this Mach number a detached bow shock wave exists as seen in Fig. 1b. Parameters of atmosphere for different altitudes that are being investigated are presented in Table 1.

Table 1 Flight regimes and parameters of surrounding gas

Flight altitude (Km)	Flight Mach number, M = 7		
	Parameters of surrounding gas before and after the bow shock wave, respectively	Flight velocity (m/s)	

Deleted:<sup>16</sup>  
Deleted:<sup>17</sup>  
Formatted: Endnote Reference  
Formatted: Endnote Reference



	Pressure (atm)		Temperature, K		Density (kg/m <sup>3</sup> )		
0 (ground)	1	58	288	3055	1.2	6.61	2381.22
20	.08	4.64	217	2302	.12	.71	2066.96
30	.01	.58	233	2472	.01	.08	2141.81

The initial conditions of injected pyrolysis gas are given in Table 2 (see Ref<sup>18</sup>). The pyrolysis gas pressure inside the TPS may vary between 8 and 30 atm. It is assumed that the pyrolysis pressure inside the TPS is independent of the choked pressure at the TPS surface and the initial plume pressure is taken equal to 30 atm unless specified otherwise. The temperature of pyrolysis gas ranges from 800K at the inner surface to 1800K at the outer surface of pyrolysis zone. The initial temperature of plume injection is taken equal to 1000 K in the current study. The duration of an individual plume injection is taken equal to 5 microseconds.

**Table 2 Plume injection parameters**

Summary of plume injection parameters	
Pressure	30 atm
Temperature	1000 K
Density	10.45 Kg/m <sup>3</sup>
Velocity	400 m/s
Spot size	6 mm
Time of injection	5 μs

The boundary condition at the TPS surface is assumed to be adiabatic in the current study. The heat transfer is evaluated by the temperature gradient at the wall caused by convected plumes (see sub-section C).

## B. The governing equations and the numerical method

The developed model is based on the compressible two-species Euler and Navier-Stokes equations. The model has recently been applied to modeling of multiple spots laser ablation<sup>19</sup>. The Euler equations in 2-D axisymmetric coordinates  $(x,y)$  (see Fig. 1a) are given by

$$\frac{\partial \sigma}{\partial t} + \frac{\partial w}{\partial x} + \frac{\partial g}{\partial y} = s,$$

where the vectors of conserved variables and fluxes are given by

$$\sigma = (\rho, \rho u, \rho v, E)$$

$$w = (\rho u, p + \rho u^2, \rho uv, (\rho E + p)u)$$

$$g = (\rho v, \rho uv, p + \rho v^2, (\rho E + p)v)$$

$$s = -(\rho v / y, \rho uv / y, \rho v^2 / y, (\rho E + p)v / y)$$

Variables  $\rho, u, v, E$  represent density, axial velocity, radial velocity, and total energy per unit mass, respectively.

The latter quantity is defined as:

$$E = \frac{p}{(\gamma - 1)\rho} + \frac{1}{2}(u^2 + v^2)$$

The ratio of specific heats  $\gamma$  for inviscid fluid satisfies the following equation

$$\frac{\partial \gamma}{\partial t} + \frac{\partial \gamma u}{\partial x} + \frac{\partial \gamma v}{\partial y} = -(\gamma v) / y$$

The variable  $\gamma$  is used in the current study to show the plume boundary and plume pattern<sup>24</sup>.

The effective viscous length scale can be defined as

$$l_{visc} = \sqrt{\nu \tau},$$

where  $\nu$  is viscosity and  $\tau$  is the time-scale. This method to evaluate the influence of viscous forces has been used by Quirk and Karni<sup>20</sup>. This criterion is based on the analytical solution for the penetration of boundary layer into the fluid at rest due to the impulsive motion of the plate. If viscous length scale is 2-3 orders of magnitude smaller than

Formatted: Endnote Reference

Deleted: <sup>30</sup>

the plume diameter, the dynamics of plumes can be described by the compressible inviscid Euler conservation equations for mass, momentum, and energy<sup>7,21</sup>. Comparison of viscous and inviscid solutions for plume dynamics, presented in Section D, confirms the inviscid simplification of governing equations.

The numerical method used to solve gas dynamics equations is the first-order accurate Godunov method using uniform numerical grid. The description of numerical methods useful for such simulations can be found in the earlier work by Pathak and Povitsky<sup>22,23</sup>. In the study<sup>23</sup>, the choice of the first-order accurate Godunov method from several other available methods is validated for highly under-expanded plumes. The accuracy of the code was tested and verified using the Sedov-Taylor explosion problem<sup>24</sup>.

The grid 300 x 300 is used so as the single code run takes 30 minutes in a modern PC.

### C. Plume emergence and heat transfer for flight at ground level

The flight at ground level is taken as a representative case to model the heat transfer pattern for given flight and plume conditions. Fig. 1a shows the simulated body covered with the TPS, together with the computational domain and boundary conditions. The plume emergence point is taken to be few grid cells above the stagnation point. The computed plume concentration is shown in Fig. 1b, while the distribution of pressure is shown in Fig. 1c and heat transfer at the TPS wall for the flight at the ground level is shown in Fig. 1d. A detached shock is evident, which is important in the heat transfer mechanism between the plume and the TPS (see Fig. 1c).

The intensity of heat transfer between the plume and the TPS is estimated by  $\Delta T = T_{NW} - T_w$ , where  $T_w$  is the TPS temperature for the steady flight before emergence of plume and  $T_{NW}$  is the gas temperature at the point located at the distance  $\Delta n$  (equal to the grid step) in the normal direction to the TPS at the time moment  $t$  after the plume emergence. The TPS surface is curvilinear so the  $T_{NW}$  is determined by the interpolation of temperature values at neighboring grid points. The value of  $\Delta T$  is positive if heating of the TPS surface occurs and negative if the plume cools the TPS surface. The estimates of heat transfer  $Q = \Delta T / \Delta n$  of the TPS surface heat transfer are listed in Table 3. The normalization parameter  $Q_0$  is chosen as the value of  $\Delta T$  obtained at  $t = 10 \mu s$ , which is the maximum absolute value at selected time moments for all altitudes. The values of normalized  $Q/Q_0$  are presented in Figures in the current study.

The pressure on ground level behind the shock wave (Fig. 1c) is larger than the initial plume pressure. Consequently, the plume does not depart from the wall or traverse into the domain. The plume remains attached to the TPS wall and it is dragged with the flow along the wall (see Fig. 1b). It can be seen that the heat transfer attains its peak in the vicinity of plume emergence that corresponds to the initial cold temperature of the plume. At ground level, the heat transfer due to the plume convection at the TPS surface is weak (see Fig. 1d) because the high pressure does not allow the mushroom-type plume pattern (to be observed later) to be formed. Therefore, the heat transfer observed in figure decreases rapidly as the plume is convected. The x-coordinate of the maximum heat transfer is shown in Table 3. The plume being attached to and dragged along the wall is observed for the altitude of flight up till 20 km. Hence, the above described heat transfer pattern remains the same up till 20 km. For the altitude of 20 km, the plume pattern and plume behavior change as described in the next sections.

Compared to higher altitudes discussed later, the convection of plume along the TPS is slow because the plume remains in the low-speed near-wall area. At  $t \sim 10 \mu s$ , in Fig. 1d some positive heat transfer area is observed upstream and downstream of the negative peak. This is due to the low pressure of plume that draws in the surrounding hot flow near the stagnation point.

Table 3 Normalization parameter at different altitude

Altitude (km)	Estimate of heat flux, $Q = \frac{\partial T}{\partial n}$					
	Location of peak along the wall X (m) at different time moments			Q (K/m) at different time moments		
	t~10 $\mu s$	t~22 $\mu s$	t~30 $\mu s$	t~10 $\mu s$	t~22 $\mu s$	t~30 $\mu s$



0	.0213	.0213	.0216	27.09E5	8.88E5	5.21E5
20	.0216	.0251	.0265	51.27E5	13.18E5	15.32E5
30	.0213	.0224	.0227	91.54E5	80.93E5	76.27E5

### C. Comparison of viscous and inviscid formulations for plume dynamics

In order to examine the importance of viscosity in the simulation, the plume patterns and heat transfer at 20 km are obtained by solving the inviscid Euler and viscous Navier-Stokes equations (see Fig. 2). Note that in this and subsequent figures, the plume fluid is distinguished by visualizing gamma, the ratio of specific heats. The difference between computational results obtained by two approaches is minor because the initial size of the ablative plume spot is 6 mm, whereas the boundary layer thickness is of the sub-millimeter scale. Besides, the velocity and pressure of plume injection is one order of magnitude higher than corresponding values of surrounding flow in boundary layer. Thus the plume is developing beyond the near-wall boundary layer. There is no significant difference in the plume pattern for these two formulations and hence, further simulations are performed using the Euler equations because of the lesser amount of required computational time. The peaks in heat transfer at the TPS wall (see Fig. 2 (c-d)), are similar for inviscid and viscous formulations.

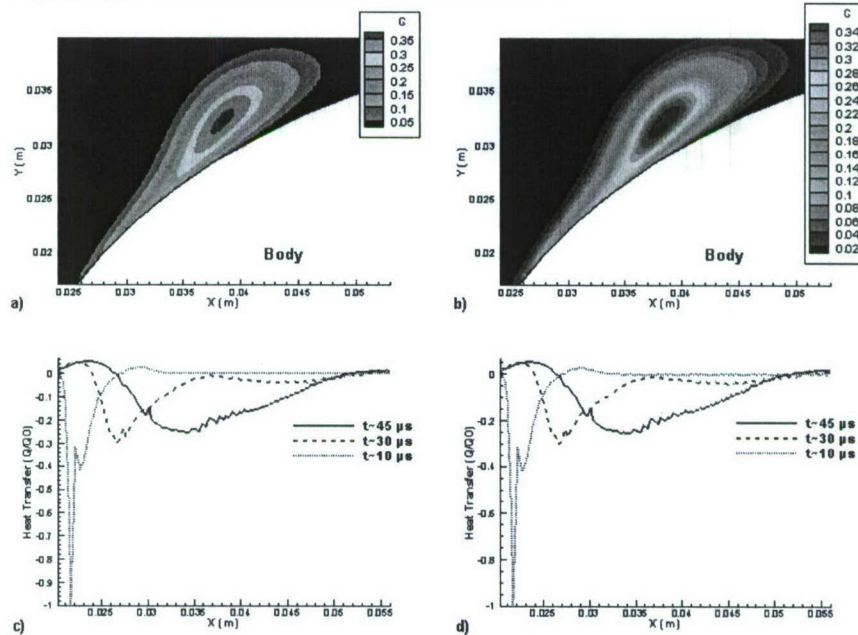


Figure 2. Comparison of viscous and inviscid models for flight at altitude 20km: a-b) plume concentration ( $t \sim 45\mu s$ ), and c-d) heat transfer coefficient, where a,c) Euler equations and b,d) Navier-Stokes equations.

### III. The effect of the flight altitude on plume dynamics and heat transfer

The altitude-dependent patterns of plume dynamics and heat transfer are discussed in this section. Fig. 3 shows the plume concentrations as the plume evolves at 20 km. The emergence of plume creates the non-uniformity in the flow behind the shock wave. At 20 km the bow shock wave remains strong (see Table 1 for pressures before and after the shock wave) and the post-shock flow can be altered only temporarily by the plume emergence. The plume core bends initially because the flow accelerates through it along the streamlined surface of the TPS. At later time moments, the acceleration of flow between the detached front shock wave and the TPS is almost uniform across the plume, as seen from the vector field in Fig. 3 (a-b). This turns the kidney-shaped plume core formed by two vortices into an oval structure (see Fig. 3c). The shape is a typical Kelvin oval formed by letting the stream flow normal to the vortex pair. This plume shape is then maintained throughout its course over the body.

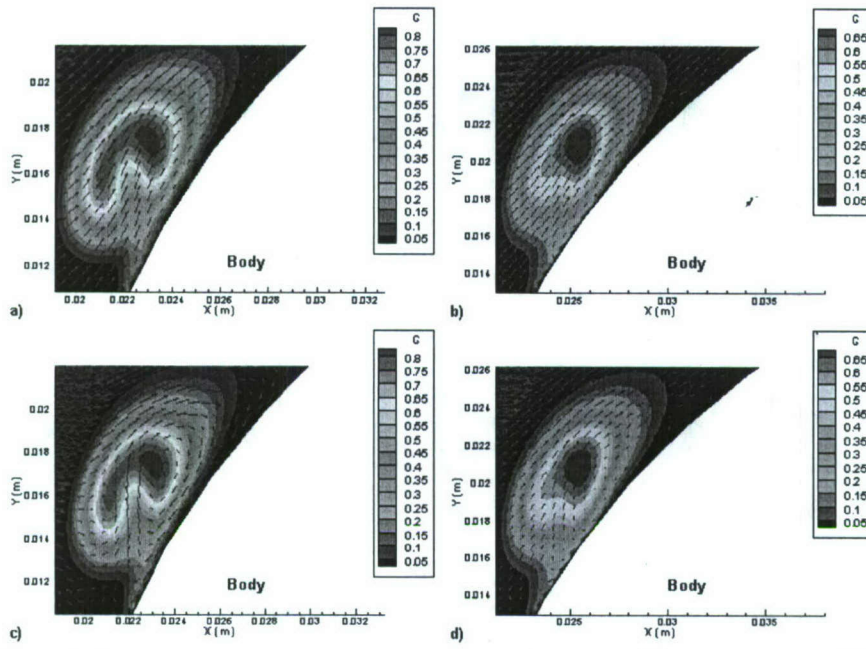
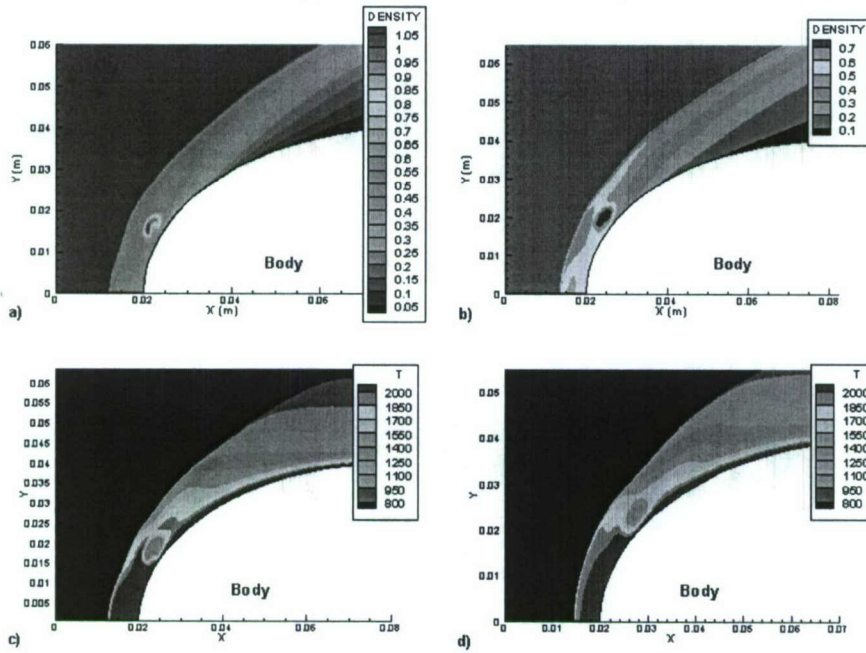


Figure 3. Plume concentration at 20 km flight altitude: a, c)  $t \sim 20 \mu s$  and b, d)  $t \sim 25 \mu s$ ; a, b) plume concentration shown with the original velocity vector field and c, d) modified vector field,  $\vec{V} - \vec{V}_{ref}$ .





**Figure 4. Plume density and temperature: a-b) density and c-d) temperature. Time moments: a-c).  $t \sim 20\mu s$  and b-d)  $t \sim 25\mu s$**

In terms of plume density, at  $t \sim 20\mu s$  (Fig. 4a) the high density in the flow field is a narrow kidney-shaped region of plume. This region is scattered after few microseconds and turns into oval as shown in Fig. 4b. Note that the area of the oval is larger than the area of the kidney-shaped plume and the density of the plume material is smaller (compare Figs. 4a and 4b). The temperature of oval-shaped plume is larger than the initial temperature of the plume (that is maintained for the kidney-shaped plume) (compare Figs. 4c and 4d). As a result, the cooling effect of the plume is diminished.

The temporarily disturbed pressure field behind the front shock wave is restored between  $20\mu s$  and  $25\mu s$  (see Fig. 4b). This restoration of pressure field gives the uniform acceleration across the plume turning the core into an oval as shown in Fig. 3 (b). In other words, the detached front shock wave smoothes any non uniformity in the flow behind the shock wave at the altitude of 20 km.

The interaction of shock wave and injection pressure wave affects the heat transfer to the body by altering the temperature field around the body. The pressure wave associated with the plume is shown in Fig. 5a. The strongest interaction of these waves occurs at the stagnation point: thus the high temperature is attained near the stagnation point. The hot gases are entrained by the plume that affects the heat transfer at TPS. Therefore, some positive heat transfer is observed around the stagnation region (see Fig. 5b).

In the later moments the heat transfer is the maximum near the plume tail when the plume is pushed back to the body by the bow shock wave as explained below. Besides, at all time moments at this altitude the modest positive heat transfer is observed around stagnation point ( $x \sim .02 m$ ). It can be seen at  $t \sim 30\mu s$  that the area with positive heat transfer around stagnation region is larger as compared to area at  $t \sim 22\mu s$ .

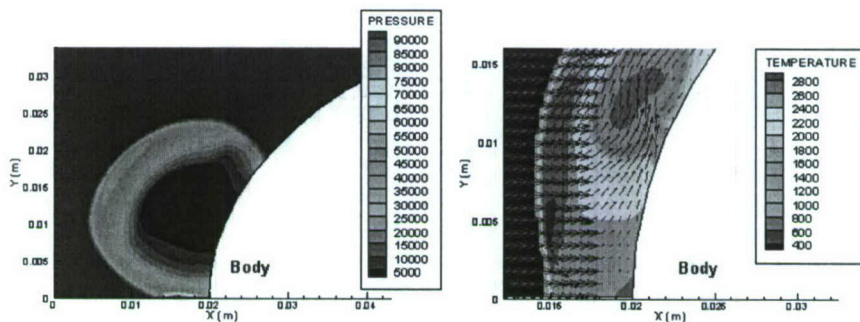


**Figure 5. Flow field near the stagnation point: a) pressure contours after plume injection over the body in still air and b) temperature contours along with the vector field for 20 km at  $t \sim 10\mu s$ .**

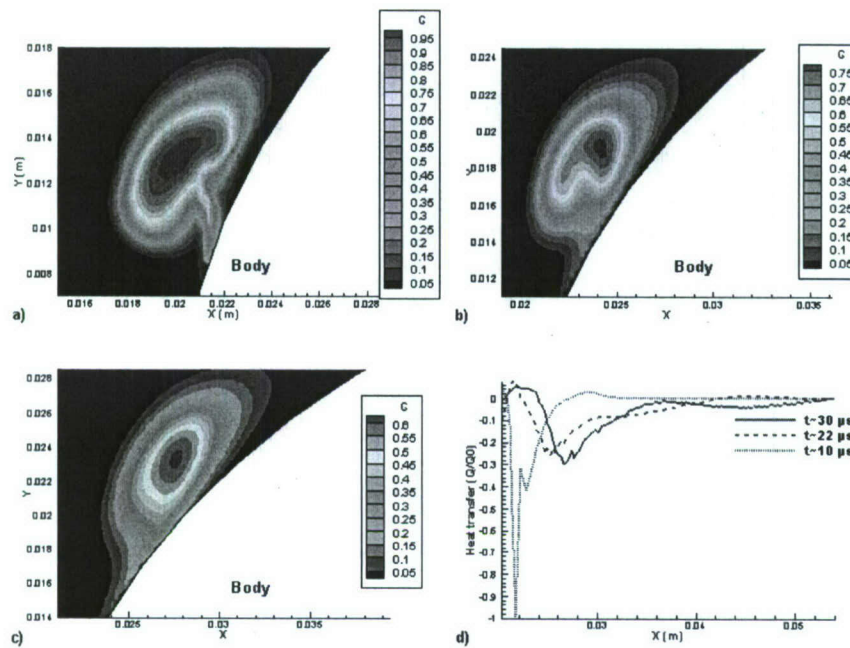


Figure 6. Plume dynamics at 20km altitude of flight: a-c) plume concentration for time moments: a)  $t=10\mu s$ , b)  $t=22\mu s$ , and c)  $t=30\mu s$ ; and d) heat transfer at the TPS wall.

In Fig. 6 the plume concentration and the heat transfer at the corresponding time moments at 20km are shown. The heat transfer is maximum (see Fig. 6 (d),  $t=10\mu s$ ) at the location of plume emergence in the initial stage of plume evolution. At later time moments the cooling heat transfer reaches its maximum near the plume tail when it touches the TPS wall. It should be noted that the peak in heat transfer is higher at  $t \sim 30\mu s$  than at  $t \sim 22\mu s$ . This occurs because the detached bow shock wave, which was distorted by the plume injection, restores and pushes the plume towards the wall. At the higher altitude of 30km, the strength of shock wave is low in terms of pressure difference across the shock wave (see Table 1) and hence the plume is able to penetrate through the shock wave as shown in Fig. 7b. By comparison of Fig. 4b and Fig. 7b, it can be seen that the emergence of plume distorts the shock wave to much larger extent at higher altitudes. The plume remains detached from the TPS and maintains its kidney shape for longer time as can be seen in Fig. 7.

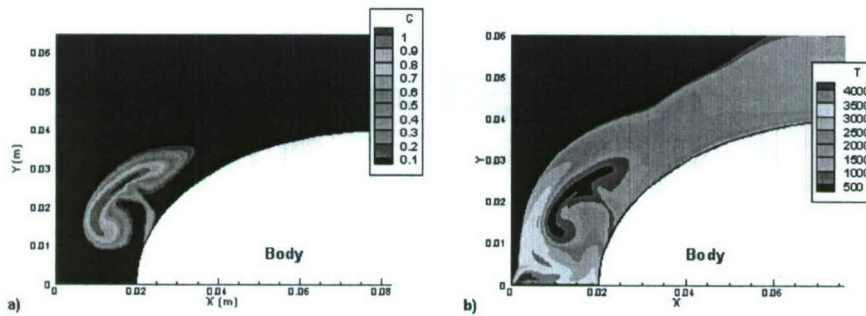


Figure 7. Plume dynamics at 30 km altitude of flight: a) plume concentration and b) density contours ( $t \sim 25\mu s$ ).

The heat transfer at 30 km is shown in Fig. 8b. At 30 km the heat transfer due to the plume convection decreases with time as the plume stays away from the wall on account of its initial high pressure (see Fig. 7). The cooling effect



is because of the interaction of the right lobe of kidney-shaped plume with the TPS wall, as shown in Fig. 7b. The temperature of the kidney-shaped plume is smaller than that for the oval plume (see discussion in the beginning of this Section); therefore, the cooling effect is more significant compared to that at 20 km. The positive maximums seen in the heat transfer graphs (Fig. 8b) are caused by the out-going pressure associated with the under-expanded plume (see Fig. 5). Unlike at the lower flight altitude of 20 km, these peaks are clearly seen downstream of the plume. In addition there is the interaction of plume-associated pressure wave with the front shock wave, as can be seen in Fig. 8a. This interaction of waves significantly affects the heat transfer.

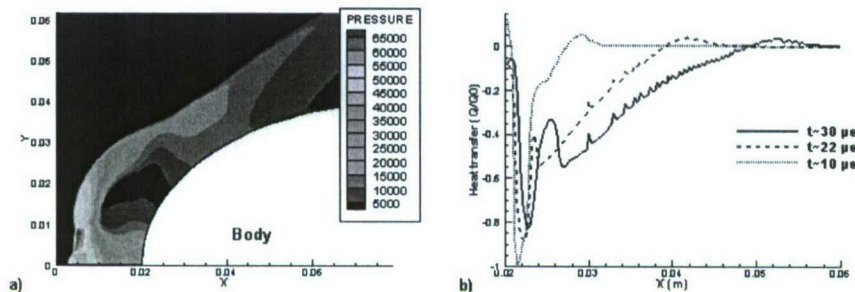


Figure 8. Interaction of waves and heat transfer at the altitude of flight of 30 km: a) pressure contours ( $t \sim 22 \mu s$ ) and b) heat transfer at wall.

For longer time of plume evolution at 30 km, significant heating around the stagnation region of the body is observed. In Fig. 9, pressure contours and heat transfer for the corresponding time moments are shown. It can be observed in Fig. 9d that there are noticeable positive peaks (heating) at the TPS surface. This heating is increased with time. The heating is caused by the shock wave associated with plume emergence. This shock wave interacts with the bow shock wave and reflects back on the TPS (see Fig. 9 (a-c)). In Fig. 9a, the bow shock wave is displaced momentarily due to this interaction and small reflection. This reflection and formation of secondary shocks is more pronounced at later time moments as seen in Fig. 9 (b-c). These secondary shock waves cause increased heating in the stagnation region.

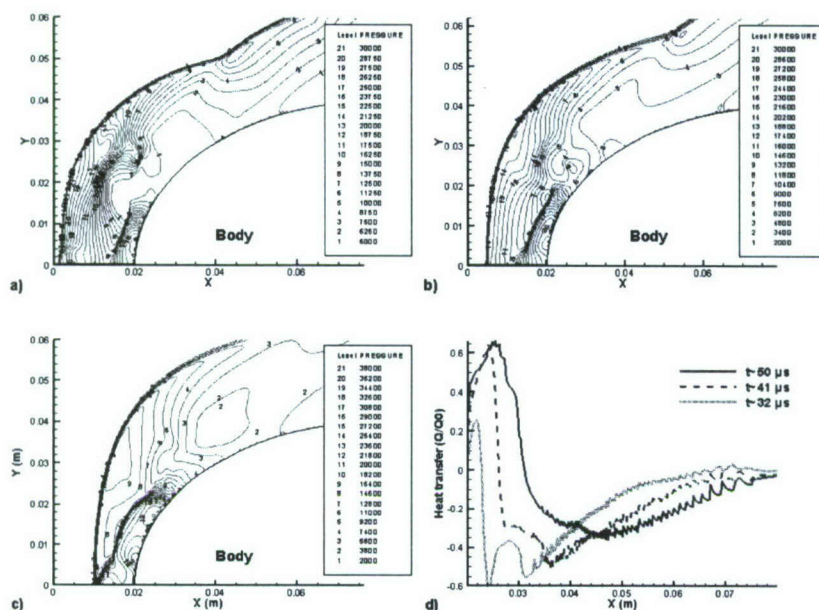


Figure 9: Formation of secondary shock waves: a-c) pressure contours; a)  $t=32\mu s$ , b)  $t=41\mu s$ , and c)  $t=50\mu s$  and d) heat transfer at the TPS wall.

In summary, at all altitudes, the temperature of emerging plume gives the normalization coefficient for heat transfer, that corresponds to the maximum (cooling) heat transfer rate at that altitude. The intensity of cooling heat transfer along the TPS wall at later time moments is determined by the plume convection. The location of maximum cooling effect is the farthest downstream for the flight at 20km altitude and is associated with the tail of the plume. At ground level, the convection is relatively slow whereas at 30km of altitude the plume propagates farther in the direction perpendicular to the TPS wall and the primary cooling is associated with one lobe of the kidney-shaped structure.

Apart from cooling, some heating effect is observed at all altitudes. Except at the ground level, this heating is caused by the out-going pressure wave due to the under-expanded plume injection. At 20 km flight altitude this effect is modest around stagnation region, whereas at 30 km of flight altitude the significant effect of this pressure wave is seen upstream and downstream of the plume over significantly larger area of the TPS. At later time moments the reflections of out-going pressure wave causes significant heating at stagnation region. This heating becomes more significant than cooling due to plume convection (see Fig. 9d).

#### IV. Heat transfer for the range of plume injection pressures



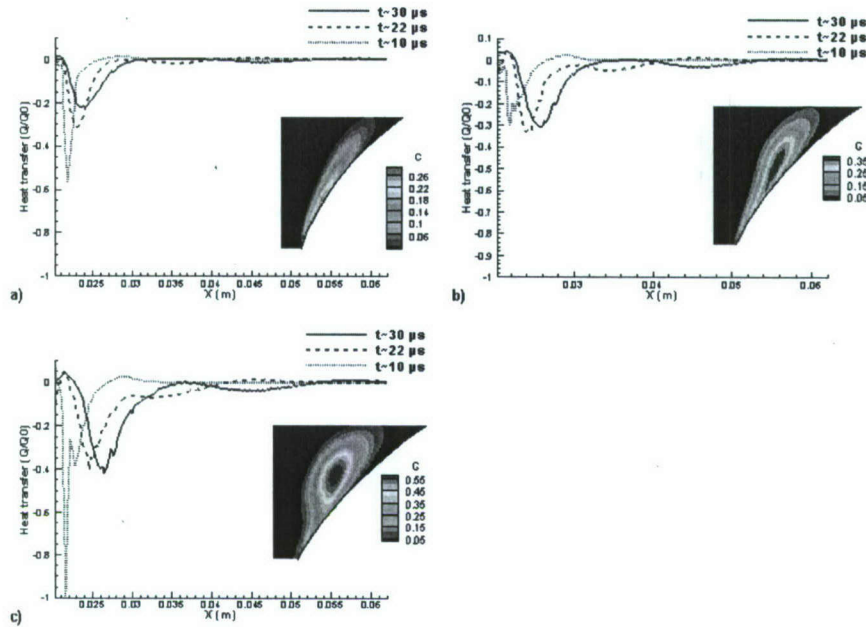


**Figure 10. Heat transfer with inset image of plume concentration at  $t \sim 30 \mu s$  for the range of initial plume injection pressures: a) 8 atm, b) 16 atm and c) 24 atm.**

The heat transfer for three different plume injection pressures is shown in Fig. 10 at 20 km flight altitude. Initial temperature of the injected plume is the same for all considered cases. The heat transfer between plume and the TPS appears to be different for these injection pressures. In Fig. 9, the normalization parameter  $Q_0$  for all considered injection pressures is taken equal to the value attained at  $t \sim 10 \mu s$  for 24 atm injection pressure. The maximum cooling heat transfer occurs at  $t \sim 10 \mu s$  for all injection pressures except for 16 atm, where the highest cooling location moves downstream, but peak values do not change significantly (in this case the maximum is observed  $t \sim 22 \mu s$ ). The peak heat transfer is largest for 24 atm.

With increasing injection pressure, the plume propagates farther away from the surface driven by its initial pressure. This is shown in the inset image of plume concentration in Fig. 10. For higher injection pressure of 24 atm (see Fig. 10c) the plume core is separated from the TPS surface thus reducing the heat convection. For 24 atm the peak in heat transfer increases at  $t \sim 30 \mu s$ , unlike the smaller injection pressures where the peak decreases with time (see Fig. 10a,b). This increase in heat transfer is caused by the high density plume which is pushed closer to TPS by the recovering detached shock wave at this time moment. For low injection pressure of 8 atm, the rate of heat transfer decreases fast with time (see Fig. 10a). Compared to higher pressures, the plume has a lower level of concentration (see inset image in Fig. 10a) indicating that the low-pressure plume mixes faster with surroundings. The maximum heat transfer for injection pressure of 16 atm is attained at  $t \sim 22 \mu s$  and the peak in heat transfer shows no significant change in time.

Overall, for low injection pressure of plume the dynamics resembles one corresponding to the flight at ground level (see Section 2D). The plume is dragged along the TPS wall, the convection rate and convective speed of plume are relatively slow, and heat transfer diminishes faster than for larger injection pressures. For higher injection pressures the plume convection can be more important for later time moments. For intermediate plume injection pressure of 16 atm the heat transfer rate is relatively steady in time. The magnitude of heat transfer is the largest for high pressure plume of 30 atm for all time moments.

## V. Heat transfer for multiple plume injections

Ejection of multiple high-pressure under-expanded plumes may appear as a sequence of increasingly complex scenarios including multiple plumes originating from the same location and multiple spatially distributed plumes. This section is focused on the interaction of plumes and interaction of pressure waves originating from the ejection of under-expanded plumes for a representative case of a pair of consecutively emerging plumes.

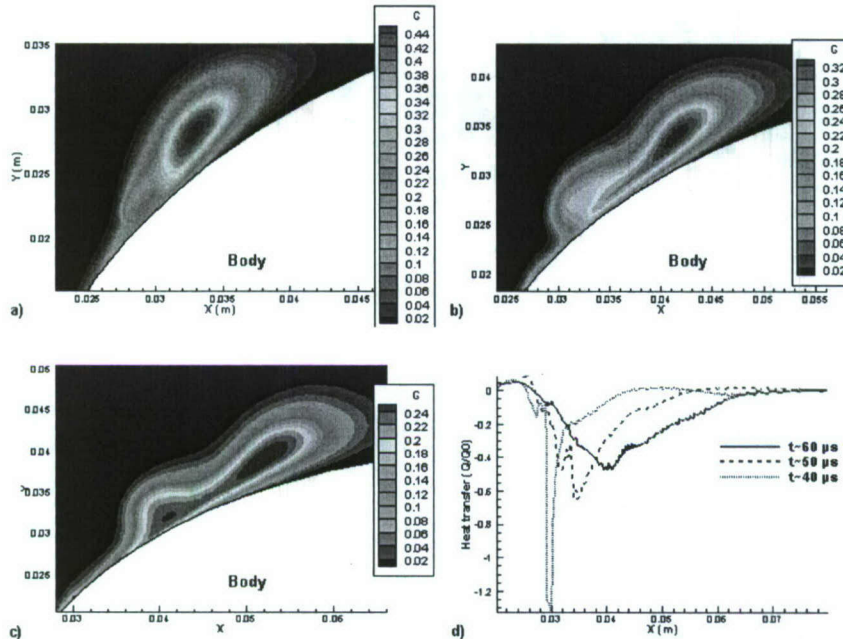


Figure 11. Emergence of two consequent plumes at 20km altitude of flight: a,b,c) plume concentration at time a)  $t=40\mu s$ , b)  $t=50\mu s$  and c)  $t=60\mu s$  and d) heat transfer at the wall.

Fig. 11 shows plume pattern and heat transfer for two plumes when the second plume emerges at the tail of the first plume at  $t=35\mu s$  after emergence of the first plume. The TPS area in contact with the tail of the first plume may have largest thermal stress because of fast cooling that causes formation of cracks and emergence of the second plume. The normalization parameter  $Q_0$  for heat transfer is the value obtained for at  $t \sim 10\mu s$  after the injection of first plume (see Table 3). For later time moments the peak in heat transfer is observed at the location of the tail of new injected plume (see Fig. 11). These locations are  $x \sim .035$  for  $t \sim 50\mu s$  and  $x \sim .04$  for  $t \sim 60\mu s$ . For these later time moments the heat transfer is dominated by the second plume convection and its pattern is similar to what is observed for single plume. It should be noted, however, the magnitude of peak cooling heat transfer is greater than unity for multiple plume injections because the second plume emerges into the first cold plume. This shows that the intensity in heat transfer increases with new plume injections.

The positive heat transfer pattern upstream of the plume injection is qualitatively similar to that for the single plume injection. As discussed before, these positive peaks were created by the propagation of plume pressure wave and its interaction with the detached front shock wave. This pressure wave is able to heat up the flow around the stagnation region (see Fig. 11d at  $x \sim .02m$ ).

## VI. Heat transfer for different TPS shapes of comparable sizes

The heat transfer and density contours for plume injection for two different body shapes are shown in Fig. 12. In the case A, the body is formed of a segment of an ellipse and in the case B it is formed by a segment of a circle connected to a straight line making the angle of 10 degrees with the horizontal axis. The former shape is the same as



described earlier in this report, while the latter body shape corresponds to the first test case in Ref. <sup>17</sup> and is typical of earth re-entry vehicles used for planetary missions.

Deleted: <sup>23</sup>

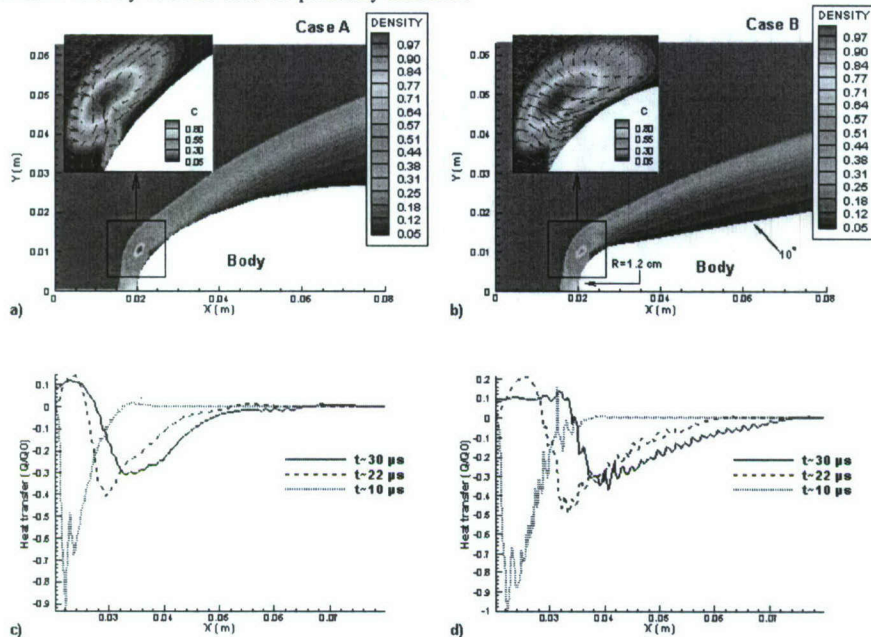


Figure 12. The effect of TPS shape at 20km altitude of flight: a-b) density contours at  $t \sim 10 \mu s$  with inset image showing plume concentration and modified vector field, and c-d) heat transfer at the TPS wall.

The normalization parameter  $Q_0$  for heat transfer is the value obtained at  $t \sim 10 \mu s$  in the case B. It can be seen from the heat transfer that the maximum heat transfer is obtained for the case B. The heat transfer peaks observed in the both cases at  $t \sim 22 \mu s$  and  $t \sim 30 \mu s$  appear due to the convective heat transfer of plume with the TPS. In the case B these peaks are observed for  $x \sim .033 m$  and  $x \sim .041 m$ , respectively; whereas in the case A, these peaks are observed for  $x \sim .029 m$  and  $x \sim .033 m$ , respectively. This indicates that the plume travels faster in the case B because of higher pressure and velocity gradients along the TPS surface that accelerates the plume. In the case A the flow is similar to that about the front portion of the sphere whereas in the case B the flow similar to impinging flow into the flat plate prevails at the front TPS surface. These body gradients in case B provide large area of vortical structures.

The plume patterns are shown in the inset image of Fig. 12. The vector field  $\vec{V} - \vec{V}_{ref}$  is plot to show the vortices by subtracting the velocity at a given point in the plume head for the respective plumes. It can be seen from the figure that the vortical structure is larger in case B that causes more intense mixing. In both cases positive heat transfer occurs upstream of plume for  $t \sim 22 \mu s$  and  $t \sim 30 \mu s$ . This is due to the pressure wave associated with plume emergence. In the case B the strength of front detached shock is comparatively low because the body is more streamlined. The initial strength of plume pressure wave is the same in both cases; consequently this wave alters the flow field to a larger degree in the case B as compared to the case A.

## VII. Conclusions

Simulations are performed to explore the effect of plumes formed through pyrolysis. The effects of plume ejection pressure, flight altitudes, body shapes and multiple plumes emergence are described. The altitude of the flight significantly affects the heat transfer between the emerging plume and the TPS. The pressure difference for the bow

shock wave is higher for lower altitudes. At high altitude the plume distorts the shock wave completely and the flow field behind the shock wave is changed significantly after the plume emergence. At low altitude the pressure behind the shock wave is high enough that the plume is unable to eject away from the wall and propagates along the TPS wall. At moderate altitudes of 20km the plume distorts the shock wave temporarily due to interaction with the plume. For the given injection conditions of relatively cold pyrolysis gas, the simulation results show no significant difference between plume patterns obtained by the Euler and Navier-Stokes equations.

The plume propagates the farthest distance along the TPS wall at moderate altitudes. Initially a kidney-shaped structure is obtained, which then evolves into an oval shape and approaches the TPS wall after being pushed back by the recovering bow shock wave. Consequently, the maximum cooling by the plume tail occurs farther away from stagnation point compared to the low and high altitudes. At high altitude, the plume propagates farther away of the TPS and maintains its double kidney shape. The cooling then occurs by interaction of one of plume lobes with the TPS.

The cooling effect is larger for the high altitude of flight because the temperature of the kidney-shaped plume remains cold. During the transformation of plume from kidney shape to oval its temperature rises and therefore the cooling effect is lesser for the moderate altitude of flight. Apart from cooling, some heating effect is observed at all altitudes. Except at the ground level, this heating is caused by the out-going pressure wave due to the under-expanded plume injection. At 20 km flight altitude this effect is significant around stagnation region, whereas at 30 km of flight altitude the effect of this pressure wave is seen upstream and downstream of the plume over significantly larger area of the TPS. At 30 km flight altitude the heating effect due to this wave is more pronounced than the cooling effect at later time moments.

The heat transfer is investigated for different injection pressure of plume. Despite the fact that the plume is detached from the TPS for higher plume injection pressures, the heat transfer between the plume and the TPS is the most intense in this case. This is caused by the plume convection in later time moments when plume is repelled by the bow shock wave toward the TPS.

For multiple plumes, it is observed that the emergence of second plume increases the magnitude of heat transfer. The behavior of heat transfer for bodies with different geometry but comparable sizes shows that the heat transfer due to plume injection is lower for body with larger radius of curvature, i.e., with more smooth geometry. The heating effect due to the plume pressure wave is higher for a body that has lower strength of front detached shock.

## References

- <sup>1</sup> F. S. Milos and Y.-K. Chen, Comprehensive Model for Multicomponent Ablation Thermochemistry, AIAA Report 97-0141.
- <sup>2</sup> S. P. Schneider, Flight Data for Boundary-Layer Transition at Hypersonic and Supersonic Speeds, *Journal of Spacecraft and Rockets*, Vol. 36, No. 1, 1999.
- <sup>3</sup> K. Komurasaki and G. V. Candler, Theoretical Consideration on Laminar-to-turbulent Transitions over an Ablating Reentry Capsule, *The Institute of Space and Astronautical Science*, 3-1-1, Yoshinodai, Sagami-hara, Kanagawa 229-8510, Japan, Report SP # 17, 2003 pp. 110-132.
- <sup>4</sup> J.-M. Bouilly et al, Design of Thermal Protection Systems for Reentry Vehicles. A Survey of Calculation and Characterization Techniques used by Aerospatiale, *Space Technology*, Vol. 18, No. 3, 1998, pp. 99-108.
- <sup>5</sup> T. Yamada, Y. Inatani, M. Honda, and K. Hirai, Development of Thermal Protection System of the MUSES-C /DASH Reentry Capsule, *Acta Astronautica*, Vol. 51, No 1-9, 2002, pp. 63-72.
- <sup>6</sup> N. Mullenix and A. Povitsky, Exploration of Pulse Timing for Multiple Laser Hits within a Combined Heat Transfer, Phase Change, and Gas Dynamics Model for Laser Ablation, *Applied Surface Science Journal*, Vol. 253, No. 15, 2007, pp. 6366-6371.
- <sup>7</sup> D. Lobao and A. Povitsky, Single and Multiple Plume Dynamics in Laser Ablation for Nanotube Synthesis, *AIAA Journal*, Vol. 43, No 3, 2005, pp. 595-608.
- <sup>8</sup> S. A. Berry and H. H. Hamilton, Discrete Roughness Effects on Shuttle Orbiter at Mach 6, AIAA report 2002-2744, 32<sup>nd</sup> AIAA Fluid Dynamics Conference, June 2002, St. Louis, MO.
- <sup>9</sup> H-K Ahn, Ch. Park, and K. Sawada, Response of Heatshield Material at Stagnation Point of Pioneer-Venus Probes, *Journal of Thermophysics and Heat Transfer*, Vol. 16, No. 3, 2002, pp. 432-439.
- <sup>10</sup> B. Vancrayenest, Investigation of the Thermochemistry of Ablation of Graphite for Planetary Entry Applications, Ph.D. Research Abstract, <http://www.vki.ac.be/research/themes/survey2004pdf/ar13.pdf>.



- <sup>11</sup> B. Vancraynest and D. G. Fletcher, Investigation of the Thermochemistry of Ablation of Graphite for Planetary Entry Applications, AIAA Report 2005-5062, presented at the 38<sup>th</sup> AIAA Thermophysics Conference, Toronto, Canada, June 2005.
- <sup>12</sup> G. Duffa et al., Ablation of carbon-based material: Investigation of roughness set-up from heterogeneous reactions, International Journal of Heat and Mass Transfer, Vol. 48, 2005, pp. 3387-3401.
- <sup>13</sup> S. Tang et al., Mechanical and ablation properties of 2D-carbon/carbon composites pre-infiltrated with a SiC filler, Carbon, Vol. 44, 2006, pp. 2877-2882.
- <sup>14</sup> Y. Aspa, et al., Identification of microscale ablative properties of C/C composites using inverse simulation, AIAA Report 2006-2911, presented in the 9<sup>th</sup> AIAA/ASME Joint Thermophysics and Heat Transfer Conference, 2006, San Francisco, CA.
- <sup>15</sup> M. Grujicic, C. L. Zhao, E.C. Dusel, D. R. Morgan, R.S. Miller and D.E. Beasley, Computational analysis of the thermal conductivity of the carbon-carbon composite materials, Journal of Material Science, Vol. 41, 2006, pp. 8244-8256.
- <sup>16</sup> Columbia Accident Investigation Board Report, Vol. 1, Limited First Printing, August 2003, by the Columbia Accident Investigation Board, Subsequent Printing and Distribution by the National Aeronautics and Space Administration and the Government Printing Office, Washington, [http://www.nasa.gov/columbia/home/CAIB\\_Vol1.html](http://www.nasa.gov/columbia/home/CAIB_Vol1.html), cited December 19<sup>th</sup>, 2007.
- <sup>17</sup> Y. Chen and F. Milos, Finite-rate ablation boundary conditions for a carbon-phenolic heat-shield, AIAA 2004-2270, 37<sup>th</sup> AIAA Thermophysics conference, Portland, Oregon, 2004.
- <sup>18</sup> H-K Ahn, Ch. Park, and K. Sawada, Response of Heatshield Material at Stagnation Point of Pioneer-Venus Probes, Journal of Thermophysics and Heat Transfer, Vol. 16, No. 3, 2002, pp. 432-439.
- <sup>19</sup> I. Zinovik and A. Povitsky, Modeling of vapor-droplet plumes ablated from multiple spots, Applied Surface Science, Vol. 253, 2007, pp. 6371-6376.
- <sup>20</sup> J. J. Quirk and S. Karni, On the dynamics of a shock-bubble interaction, J. Fluid Mech., Vol. 318, 1996, pp. 129-163.
- <sup>21</sup> F. E. Marble, Dynamics of Dusty Gases, Annual Review of Fluid Mechanics, Vol. 2, 1970, p. 397.
- <sup>22</sup> K. Pathak and A. Povitsky, Inviscid, Viscous and Turbulent Models of Plume Dynamics for Laser Ablation of carbon, J. Computational and Theoretical Nanoscience, Vol. 3, No. 4, 2006, pp. 565-578.
- <sup>23</sup> K. Pathak and A. Povitsky, Inviscid, Modeling of plume dynamics with shielding in laser ablation of carbon, Applied Surface Science, Vol. 253, 2007, pp. 6359-6365.
- <sup>24</sup> I. Zinovik and A. Povitsky, Dynamics of multiple plumes in laser ablation: modeling of the shielding effect, J. Appl. Phys., Vol. 100, 024911, 2006.